ICAS 2020 SHANG HAI
International Council of the Aeronautical Sciences
32nd Congress of the International Council of the Aeronautical Sciences
September 6-10, 2021
Pudong Shangri-La, Shanghai, China

Numerical Investigation of Nacelle Intake Flow Distortion at Crosswind Conditions

Mai ZHANG[1]

[1]AECC Commercial Aircraft Engine Ltd, Shanghai, 200241

Abstract

The intake flow distortion at crosswind conditions of the nacelle of a representative high-bypass ratio turbofan engine is investigated, considering influence of several operating parameters: the aircraft rolling speed, the intake massflow rate and the crosswind velocity magnitude. The steady-state Reynolds-averaged Navier-Stokes equations are solved to obtain the flow field. The results show that the occurrence of the ground effect vortex depends on whether the intake streamtube touches the ground. Regarding ground rolling speed, it is shown that a small forward rolling speed could eliminate the inlet distortion caused by the ground effect, as the rolling speed would reduce the intake streamtube cross-sectional area and elevates the bottom of the streamtube from the ground. Regarding intake massflow rate, four flow phenomena are observed subsequently as the intake massflow rate increases from the lowest to the highest values: nacelle lip subsonic flow separation, lip separated-flow reattachment, the ground effect and the nacelle lip shock-induced boundary-layer separation. These phenomena constitute the mechanisms that explain the way the distortion level changes with increasing intake massflow rate. With regard to the crosswind velocity magnitude, this parameter affects the cross-sectional area of the intake streamtube as well as the tendency of flow separation at the nacelle lip, thereby affecting the intake massflow rates at which both the ground effect and the lip flow separation occur.

Keywords: Inlet Distortion, Crosswind, Ground Effect, Nacelle

1. Introduction

The crosswind condition presents a challenge to the design of the nacelle for modern high bypass-ratio turbofan engines. In this condition, intake flow distortion is likely to occur, due to nacelle lip flow separation and the ground effect. The intake flow distortion, usually measured in terms of total pressure loss and swirl, constitutes the aerodynamic excitation in the fan blade forced response problem as well as reducing the aerodynamic stability of the fan and the compressor [1,2]. Additionally, the ground effect may cause foreign object ingestion damage to the engine [3] and flow field condensation [4].

The ground effect in the crosswind conditions is characterized by a ground vortex between the nacelle and the ground, as observed in real situation or experiment (e.g. Figure 1, [5]). The ground effect has been a focus in existing crosswind investigations as most of the detrimental crosswind scenarios occur when the ground effect is present when the aircraft is operating on the ground. Zantopp et al. [6] showed that the crosswind flow can be complicated, in which the ground vortex, the nacelle lip flow separation, and additional vortices trailing from the nacelle outer surface can appear at the same time and interact with each other. Kline [7] stated three necessary conditions for the ground effect to occur, i.e. the non-zero ambient vorticity, a stagnation point on the ground, and an ascending flow from the stagnation point to the nacelle intake. De Siervi [8] showed that the formulation mechanism of the ground effect in the crosswind conditions is different from that in the headwind conditions, and is not linked to the ambient vorticity. Murphy et al. [9] identified two key parameters that govern the occurrence and strength of the crosswind ground effect vortex: the ratio between the free-stream velocity and the engine inlet flow velocity, and the ratio between the

nacelle-ground distance and the intake diameter.

Figure 1 – Ground effect vortex observed in a wind tunnel model experiment [5]

Understanding the crosswind inlet distortion mechanisms is fundamental to the design of a well-performed nacelle that maintains proper engine operation in crosswind conditions and meets air-worthiness requirements. Moreover, it also helps to improve fan blade design in terms of aerodynamic stability and the forced response problem. The present paper aims to contribute to the understanding of the crosswind inlet flow distortion by numerical studies for a nacelle that resembles realistic geometry. The results will be split into sections concerning the influence of several key operating factors: the aircraft ground rolling speed, the intake massflow rate, and the crosswind velocity magnitude. The focus of this work is to identify the key flow field phenomena and analyze the mechanisms underlying the inlet distortion in these crosswind conditions.

2. Case to Study

The crosswind conditions are based on realistic ground operating points, i.e. when the aircraft is resting or rolling on the ground. A baseline crosswind condition, as listed in Table 1, is specified as the starting point for generating other crosswind conditions by changing the relevant parameters. In the baseline condition, the freestream condition is based on the international standard atmosphere (ISA) [10] at sea level. The bottom of the nacelle outer surface is in realistic clearance above the ground. The crosswind velocity vector is defined in the ground stationary reference frame, and is set as 90 degrees from the engine axis, with a crosswind magnitude of 35 knots, as typically considered in the engine certification process.

Table 1 The baseline crosswind condition

Crosswind direction	Crosswind velocity magnitude	Aircraft rolling Mach number Ma_x	Altitude	Freestream conditions	Intake massflow rate
90 degrees from the engine axis	35 knots	0	0 meter	1 atm, 288.15K	Maximum take-off

The inlet distortion is quantified by a single number, the IDC_{max}, based on the SAE ARP1420B standard [11] on the AIP plane. According to the standard, the AIP plane is split into five rings with equal areas from the hub to the casing. Each ring is placed with eight probes distributed uniformly in the circumferential direction at the averaged radius of the ring, amounting to a total of 40 probes, as shown in Figure 2. Additionally, however, to better align the probe with the location of the ground effect vortex, in this work all the probes are further rotated by 22.5° around the engine axis during post-processing the simulation results. The IDC_{max} is calculated as:

$$IDC_{max} = max_{i=1}^{4} \left(0.5(IDC_i + IDC_{i+1})\right) \quad (1)$$

in which, IDC_i is defined as,

$$IDC_i = \frac{p_{t,avg,i} - p_{t,min,i}}{p_{t,avg,face}} = \frac{\sigma_{avg,i} - \sigma_{min,i}}{\sigma_{avg,face}} \quad (2)$$

where $p_{t,avg,i}$ and $p_{t,min,i}$ are the arithmetic average and the minimum of the absolute total pressure p_t of the eight probes on the i-th ring, and $p_{t,avg,face}$ is the arithmetic average of the absolute total pressure of the 40 probes on the AIP plane. σ is the total pressure recovery coefficient, which is the absolute total pressure normalized by the freestream absolute total pressure,

$$\sigma = \frac{p_t}{p_{t,\infty}} \quad (3)$$

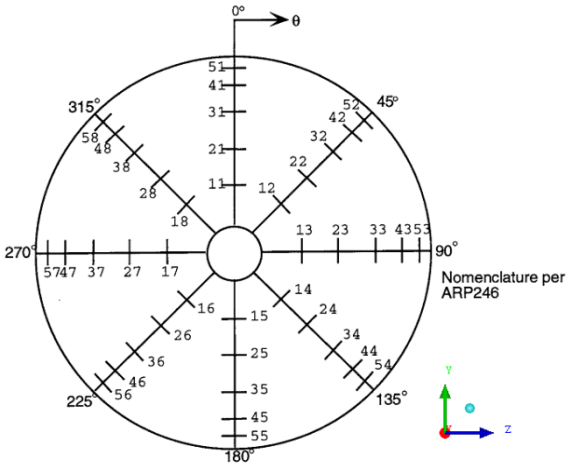

Figure 2 – Positions of the probes on the AIP plane based in the ARP1420B standard

3. Computational Methods

The computational domain consists of five far-field boundaries and a ground plane, as shown in Figure 3. The ground plane is modeled with no-slip wall boundary condition and the freestream condition is prescribed on the far-field boundaries with values for Mach number, static temperature, and the crosswind flow direction in positive z-direction (i.e. 90° from the engine axis).

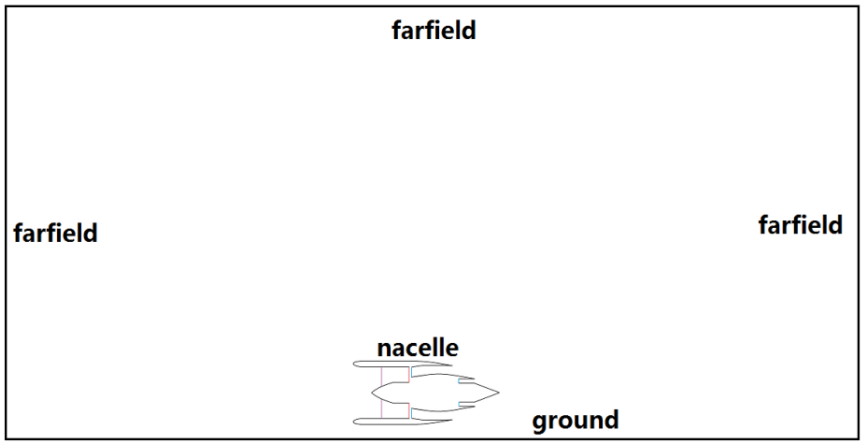

Figure 3 – Relative positions of the nacelle, far-field and ground plane in the computational domain, (size of the domain in the figure does not represent the real size used)

The boundary conditions applied on the nacelle is schematically shown in Figure 4. In the simulation,

the fan blades are not included, but the fan domain is still kept and is extended downstream until an outlet boundary. On the outlet boundary, a fixed massflow rate is specified, and the static pressure is automatically adjusted during the calculation to realize the prescribed massflow rate. At the rear part of the nacelle, the bypass and core ducts are included and are modeled as inlet boundary conditions, where the flow is assumed normal to the boundaries and the total pressures and total temperatures are specified from engine cycle calculations based on the intake massflow rate. An aerodynamic interface plane (AIP) is placed at the axial starting point of the fan domain to investigate the flow distortion caused by the nacelle.

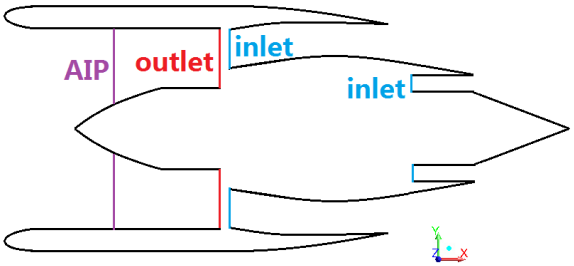

Figure4 – Schematic locations of the boundaries and the AIP plane in the calculation (shape is simplified for illustration only and does not represent the actual geometry)

The computational mesh around the nacelle and the ground is shown in Figure 5. The mesh consists of hexagonal cells with resolution concentrated to the areas where the flow is expected to be complicated. These areas are the front part of the nacelle, the nacelle lip, the space between the ground and the bottom of the nacelle, and the direction normal to the ground plane. The resolution of the mesh and the distance of the far-field are determined based on previous mesh dependence study, resulting in 13 million cells in total and the far-field boundaries placed 20 nacelle diameters away from the engine. The mesh is refined normal to all the wall boundaries, including the ground plane, with y+ of about 5.

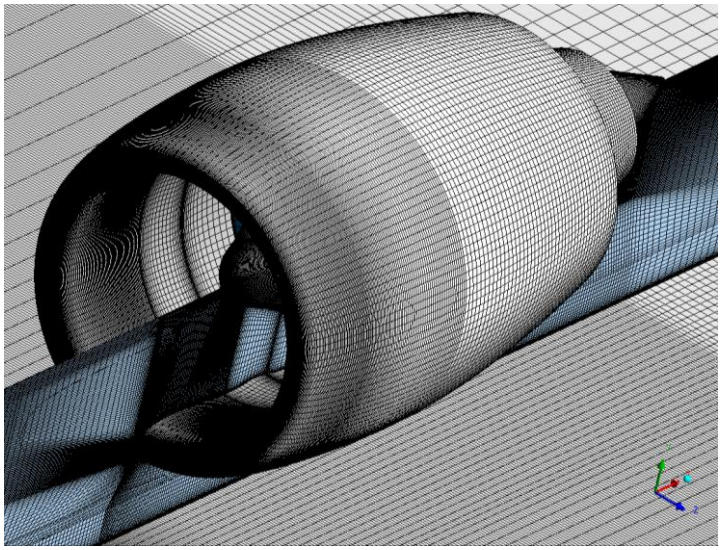

Figure 5 – Mesh resolution in the interior fluid domain (blue), on the nacelle and on the ground

The commercial solver ANSYS Fluent [12] is used to solve the compressible steady-state Reynolds-averaged Navier-Stokes (RANS) equations. The flow field is discretized spatially with second-order upwind schemes. The Spalart-Allmaras turbulence model [13] is used to model the turbulence.

4. Results and Discussion

Figure 6 shows the nacelle inlet flow field of the baseline crosswind condition (crosswind of 35 knots, 90° , 0 aircraft rolling speed). From the streamlines, it can be seen that when the crosswind reaches the entrance of the engine, a vortex forms between the ground and the nacelle, and the flow spirals into the engine, causing a total pressure distortion at the core of the vortex on the AIP

plane. Additionally, the ground plane is colored by static pressure, showing a local minimum of the static pressure at the core of the vortex. The features of the predicted streamlines and total pressure distortion is similar to typical crosswind ground effect phenomena observed in previous studies (e.g. [9]) and in real-life situations (e.g. Figure 1)

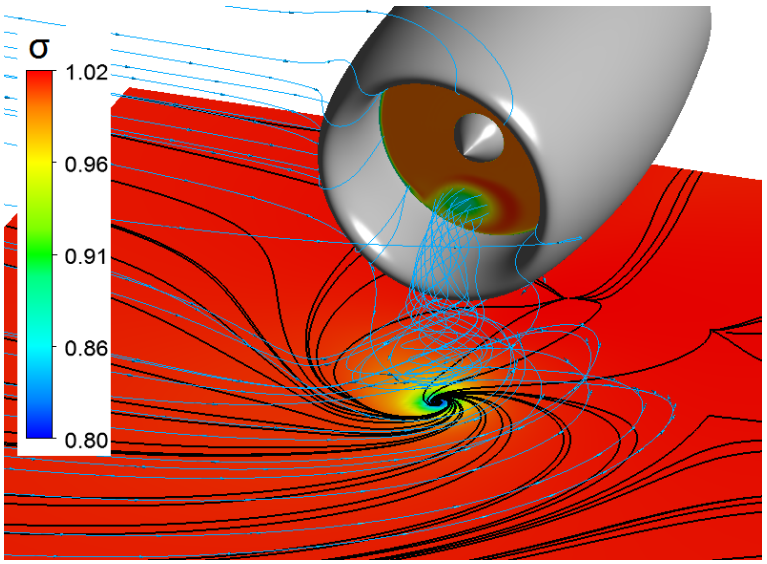

Figure 6 – The flow field and the contour of total pressure recovery $\sigma = \frac{p_{t,local}}{p_{t,\infty}}$ on the AIP plane, at the baseline crosswind condition

4.1 Effect of the Ground Rolling Speed

The effect of the aircraft rolling speed is investigated by increasing the aircraft rolling Mach number from 0 in the engine axial direction. As the computational reference frame is fixed to the nacelle, the rolling speed is modeled by specifying a wall translating velocity on the ground plane moving towards downstream of the engine. Additionally, as the crosswind velocity vector related to the ground remains unchanged at different rolling speeds, the component of the crosswind velocity vector normal to the engine axis shall be invariant relative to the nacelle, whereas the headwind component relative to the nacelle should be equal to the rolling speed such that there is no headwind component relative to the ground.

This makes the mechanisms of crosswind rolling different from the case of combined headwind and crosswind with 0 rolling speed. Though in both cases the wind has headwind component relative to the nacelle, in the case of combined headwind and crosswind with 0 rolling speed, the headwind component is moving relative to the ground and generates additional vorticity in the ground boundary layer, which would generate the quiescence/headwind ground effect mechanism (the 'first mechanism' as discussed by De Siervi [8]), whereas for the crosswind rolling case, such mechanism does not exist since the headwind component relative to the ground is zero.

To investigate the change of flow distortion with the rolling speed, measured by the rolling Mach number, simulations were run at increasing rolling Mach numbers of 0.01, 0.02, 0.03, 0.04 and 0.05. It is then found that the flow distortion is evident only until the rolling Mach number higher than 0.01 (i.e. for the rolling Mach number of 0.02 it was found that the distortion was already not evident). For the rolling Mach number of 0.01, as shown in Figure 7, the flow field is similar to the baseline condition. It can be seen that the bottom of the streamtube that enters the engine touches the ground, forming the ground vortex, and causes flow distortion on the AIP plane. For the higher rolling Mach number of 0.05, as shown in Figure 8, the freestream velocity relative to the nacelle increases, so that the cross-sectional area of the streamtube decreases, with its bottom leaving the ground, eliminating the ground effect. As a result, no vortical pattern is seen on the ground limiting streamlines and there is no flow distortion on the AIP plane. This result is consistent with previous research that the occurrence of the crosswind ground effect depends on whether the inflow streamtube touches the ground.

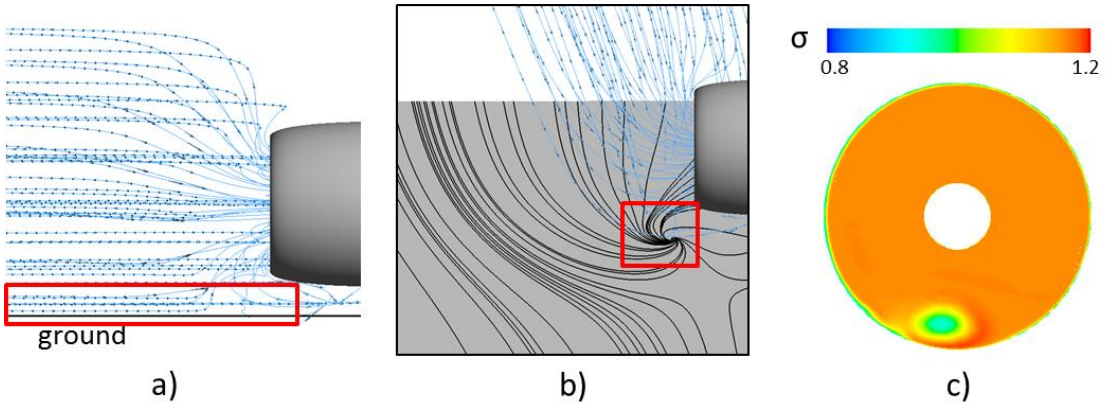

Figure 7 – Flow field at rolling Mach number of 0.01 (a) intake streamtube touches the ground (b) ground limiting streamlines showing vortical pattern (c) AIP total pressure recovery coefficient σ

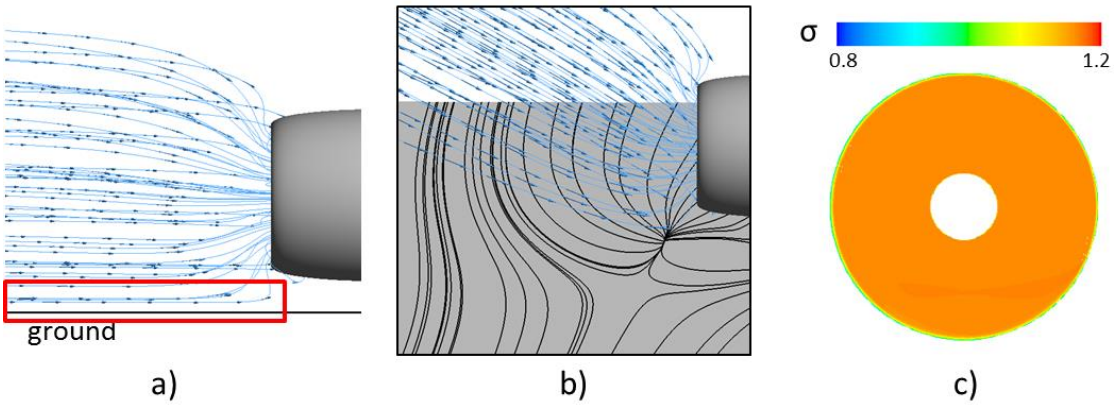

Figure 8 – Flow field at rolling Mach number of 0.05 (a) intake streamtube leaves the ground (b) no vortical pattern is apparent on the ground limiting streamline (c) clean inlet flow without distortion

4.2 Effect of the Intake Massflow Rate

The effect of the intake massflow rate is investigated by increasing the massflow rate from 10% to 110% of that of the baseline crosswind condition, for three crosswind velocity of 20 knots, 35 knots and 45 knots respectively. The variation of the contour of total pressure recovery σ on the AIP plane, as well as the variation of the distortion index IDC_{max}, as the massflow rate increase, are shown for the three crosswind velocity magnitudes respectively in in Figure 9, Figure 10 and Figure 11. The total pressure loss locally on the AIP plane is thus $1 - \sigma$. Four phenomena can be identified in the inlet distortion, as described below.

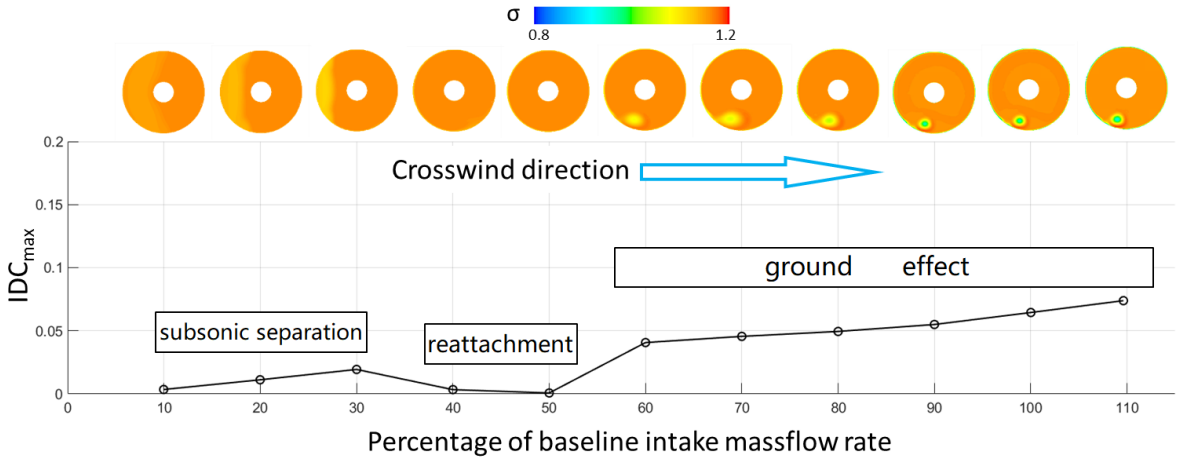

Figure 9 – Variations of inlet distortion and IDC_{max} on AIP plane with intake massflow rate, crosswind speed: 20 knots

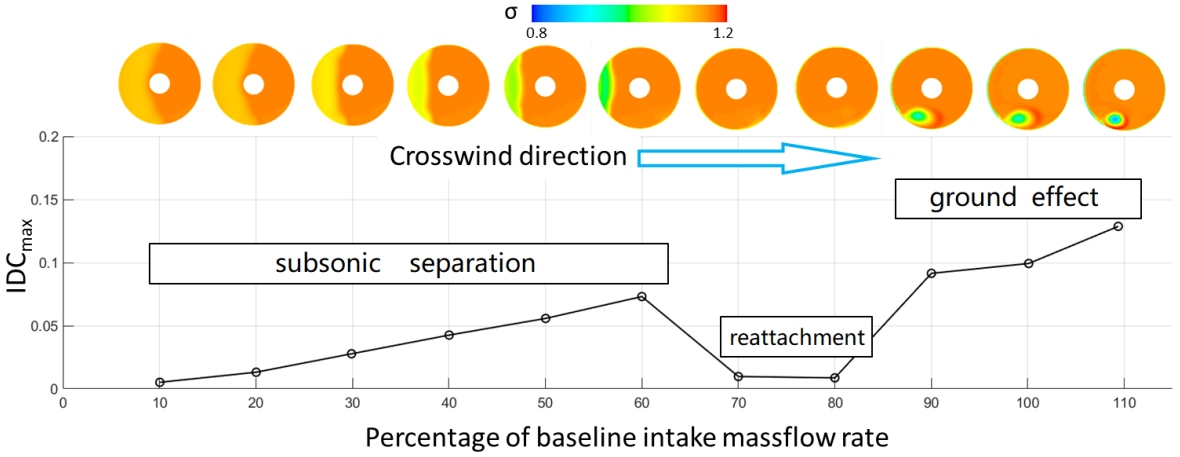

Figure 10 –Variations of inlet distortion and IDC_{max} on AIP plane with intake massflow rate, crosswind speed: 35 knots

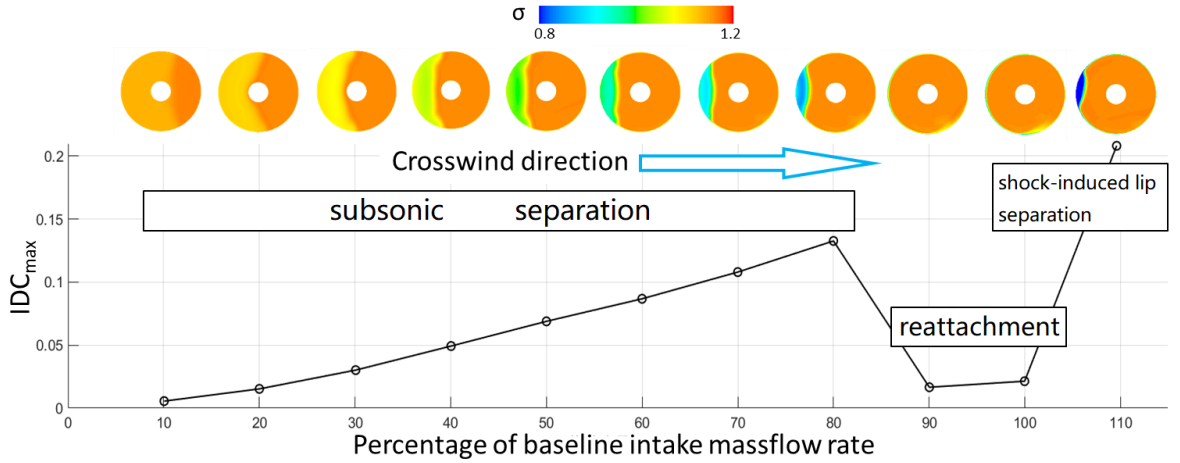

Figure 11 –Variations of inlet distortion and IDC_{max} on AIP plane with intake massflow rate, crosswind speed: 45 knots

The first phenomenon is the inlet distortion caused by subsonic flow separation at the lip of the nacelle, for example, between 10% and 60% of the baseline massflow rate (i.e. maximum-take-off) in the 35-knot crosswind case (see Figure 10). In this regime, no ground vortex is found. At 10%

baseline massflow rate, the area of the distortion can be as large as half of the AIP plane, but with very small total pressure loss (i.e. $1 - \sigma$). As the massflow rate increases, the size of the distorted region decreases but the magnitude of total pressure loss increases. The maximum local total pressure loss on the AIP plane can reach about 10% in the subsonic separation region, at the case of 60% baseline intake massflow rate. Figure 12 shows the details of the subsonic flow separation around the windward lip of the nacelle on a sectional plane, along with the contour of total pressure recovery σ on the AIP plane. It can be seen that the separation starts at the lip surface immediately after the location of highest curvature, where the flow experiences the strongest deceleration after the point of highest velocity (i.e. the lip suction peak). The separation zone is characterized by a large area of reversed flow, as shown by the arrows of the streamlines.

The second phenomenon is the reattachment of the separated flow as the massflow rate is further increased, for example, between 70% to 80% of the baseline massflow rate in the 35-knot crosswind case in Figure 10. The reattachment occurs due to the increased intake massflow that reduces the static pressure downstream of the nacelle lip and alleviate the adverse pressure gradient. Since the ground vortex is not formed yet, there are no major sources of flow distortion, so that the inlet flow becomes clean and the IDC_{max} drops close to zero.

The third phenomenon is the ground effect, i.e. the presence of the ground vortex, at higher massflow rates, for example, between 90% to 110% of the baseline massflow rate in the 35-knot crosswind case in Figure 10. The cross-sectional area of the inflow streamtube grows to accommodate more intake massflow and touches the ground. The ground vortex thus forms, causing inlet flow distortion and an increase of the IDC_{max}. The maximum local total pressure loss on the AIP can reach about 15% at the center of the vortex. The IDC_{max} caused by the ground effect also appears higher than that caused by the subsonic lip flow separation.

The fourth phenomenon is characterized by the shock-induced boundary layer separation at the nacelle lip, at the highest massflow rate and the highest crosswind speed of 45 knots, (i.e. 110% of the baseline massflow rate for the 45-knot crosswind case in Figure 11). Figure 13 shows the detail flow field around the windward lip of the nacelle on a sectional plane, along with the contour of total pressure recovery σ on the AIP plane. It can be seen that the flow has become locally supersonic at the lip at the location of the highest surface curvature. Due to the combined effects of high massflow, high crosswind speed and high lip surface curvature, the flow is accelerated to become locally supersonic and terminated by a local shockwave that is strong enough to separate the boundary layer. The resulting total pressure loss is significantly higher than that cause either by the subsonic separation or by the ground effect, with a maximum local total pressure loss reaching 32%, and the IDC_{max} as high as 0.2, as seen in the sudden rise of IDC_{max} in Figure 11.

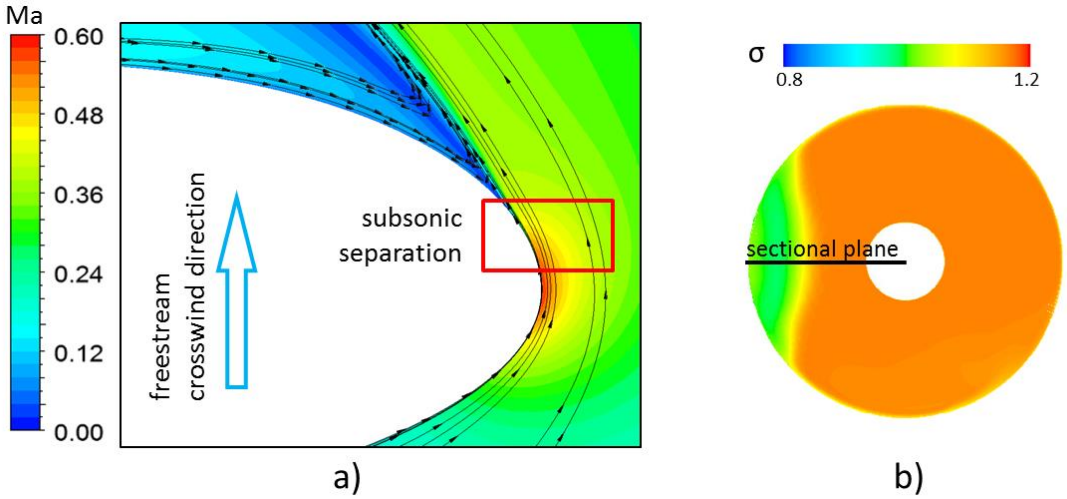

Figure 12 – (a) Mach number and streamlines around the nacelle lip on the sectional plane, indicating subsonic lip separation, at 60% massflow at 35-knot crosswind (b) circumferential position of the sectional plane

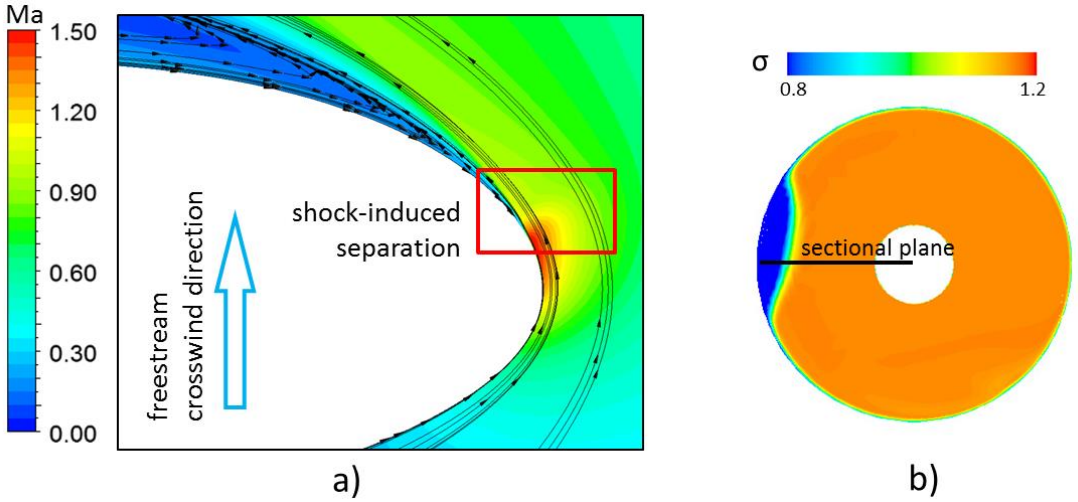

Figure 13 – (a) Mach number and streamlines around the nacelle lip on the sectional plane, indicating shock-induced lip separation, at 110% massflow at 45-knot crosswind (b) circumferential position of the sectional plane

4.3 Effect of the Crosswind Velocity Magnitude

The effect of crosswind velocity magnitude can also be examined by comparing the results from Figure 9, Figure 10 and Figure 11 above.

For the 20-knots crosswind speed case (Figure 9), the separation reattachment appears at a lower massflow rate than the baseline crosswind case (Figure 10). This is because, as the crosswind velocity is reduced, the peak of the velocity at the nacelle lip is reduced, and the adverse pressure gradient after the peak is also reduced. Thus, a lower value of intake massflow is required to reattach the flow. Additionally, the ground effect also appears at a lower massflow rate. This is because, as the lower crosswind speed reduces the intake massflow rate passed by the streamtube, the bottom of the streamtube would then touch the ground at a lower intake massflow rate. Finally, the supersonic lip separation is not observed in the 20-knots and 35-knots case, since the crosswind velocity is too low to accelerate the lip flow to be locally supersonic to cause the shock-induced boundary-layer separation.

For the 45-knots crosswind speed case (Figure 11), the separation reattachment occurs at a higher massflow rate, because the higher crosswind speed increases the peak velocity at the lip, resulting in a higher adverse pressure gradient downstream of the lip, thus requiring a higher intake massflow rate to alleviate the adverse pressure gradient to reattach the flow. The ground effect appears at a higher massflow rate, since higher crosswind speed increases the massflow rate inside the streamtube thus the streamtube would touch the ground at higher intake massflow rate. Finally, the shock-induced lip separation occurs at the highest massflow rate, due to the combined effects of high crosswind speed, high massflow, and lip surface curvature.

5. Concluding Remarks

Steady-state RANS equations are solved to investigate the flow field of a nacelle of a high-bypass ratio engine in crosswind conditions on the ground, with 90-degree crosswind relative to the engine axis. The prediction of the baseline crosswind condition shows that the crosswind would cause the ground effect, featured by a vortex spiraling into the nacelle from the ground and causes total pressure loss at the core of the vortex. The predicted flow field pattern is consistent with previous investigations and real-life scenarios.

The study shows that aircraft ground rolling can be used to eliminate the ground effect. As the rolling speed is increased, the intake streamtube shrinks so that its the bottom leaves the ground, causing the ground effect to disappear. For the present investigation at the baseline crosswind

condition, a clean intake flow without distortion can be realized with a small rolling Mach number higher than 0.01.

During the entire range of engine intake massflow rate, the crosswind inlet distortion will subsequently experience four phenomena: the subsonic flow separation at the lip, the reattachment of the subsonic flow separation, the ground effect vortex, and the shock-induced boundary-layer separation at the lip. This results in the IDC_{max} to first increase gradually, followed by a sudden drop to nearly zero, and then increases again, as the massflow rate is increased.

The effect of crosswind velocity magnitude affects the intake massflow rate at which the ground effect occurs, due to the change of the massflow rate inside the intake streamtube. Lower crosswind velocity results in a lower intake massflow rate being passed so that the streamtube touches the ground at a lower intake massflow rate, and vice visa. Additionally, the crosswind velocity magnitude affects the tendency of the subsonic lip separation and the required intake massflow rate to reattach the separated flow, as well as the occurrence of the shock-induced boundary-layer separation, since the crosswind velocity magnitude affects the maximum velocity around the lip and the adverse pressure gradient immediately downstream.

6. Acknowledgement

The author would like to thank Dr. GUO, Fushui, Dr. LIU hui and Dr. YANG zhong and Prof. LUO Guangqi at AECC CAE for their technical support and many useful discussions during this work.
The author is also grateful to AECC CAE for granting permission to publish.

7. Contact Author Email Address

mailto: zm.myron@gmail.com

8. Copyright Statement

References

[1] Motycka D, Walter W and Muller G. An Analytical and Experimental Study of Inlet Ground Vortices. *AIAA/SAE 9th Propulsion Conference*, Paper No. 73-1313, 1973.

[2] Di Mare L, Simpson G and Sayma A. Fan Forced Response due to Ground Vortex Ingestion, ASME Turbo Expo 2006, Barcelona, Spain, GT2006-90685, 2006

[3] Rodert L and Garrett F. Ingestion of Foreign Objects into Turbine Engines by Vortices, NACA Technical Report, TN-3330, 1953.

[4] Campbell JF and Chambers JR. Patterns in the Sky: Natural Visualizations of Aircraft Flow Fields, NASA Technical Report, SP-514, 1994.

[5] Brix S and Neuwerth. Untersuchungen zur Entstehung und Starke Von Triebwerkseinlaufwirbeln, Dissertation, Fakultat fur Maschinenwesen der Rheinisch-Westfalischen Technischen Hochschule Aachen, Deutschland, 2004.

[6] Zantopp S, MacManus D and Murphy J. Computational and Experimental Study of Intake Ground Vortices, The Aeronautical Journal, Voo, 114, No. 1162, 2010.

[7] Klein H. Small Scale Tests on Jet Engine Pebble Aspiration Tests, Douglas Aircraft Company Repoart, SM14885, 1985.

[8] De Siervi F. Mechanisms of Inlet-Vortex Formulation. Journal of Fluid Mechanics, Vo. 124, 1982.

[9] Murphy JP and MacManus DG. Ground Vortex Aerodynamics under Crosswind Conditions, Experiments in Fluids, Vol. 50, 2011.

[10] International Organization for Standardization, Standard Atmosphere, ISO 2633:1975, 1975

[11] SAE APR1420B, Gas Turbine Engine Inlet Flow Distortion Guidelines, 2011.

[12] ANSYS, Inc. ANSYS Fluent, Release 15.0, Help System, Theory Guide, Section 20.4

[13] Spalart PR and Allmaras SR. A One-Equation Turbulence Model for Aerodynamic Flow, AIAA Paper No. 92-0439, 1992.